Acta Astronautica 237 (2025) 174–187

Contents lists available at ScienceDirect

Acta Astronautica

journal homepage: www.elsevier.com/locate/actaastro

Research paper

Assessing control robustness of CubeSat propulsion systems for minor body proximity operations

Carmine Buonagura [a,b,*], Carmine Giordano [a], Angelo Cervone [b], Francesco Topputo [a]

[a] Department of Aerospace Science and Technology, Politecnico di Milano, Via La Masa 34, Milan, 20156, Italy
[b] Department of Space Science, TU Delft, Mekelweg 5, Delft, 2628 CD, Netherlands

ARTICLE INFO

Keywords:
Minor body
6-DoF
Guidance
Control
Propulsion
CubeSat

ABSTRACT

Exploration of minor celestial bodies is attracting increasing attention due to the scientific insights and engineering advancements it can provide. Concurrently, miniaturized platforms such as CubeSats are becoming increasingly popular because of their reduced development, qualification, and launch costs. This enables riskier operations, making them ideal for proximity operations around minor bodies. This work introduces a 6-DoF guidance and control simulation framework for proximity operations along hyperbolic trajectories near minor bodies. An optimization algorithm was designed coupling attitude dynamics with trajectory design, while directly considering performance and technological limitations of CubeSat propulsion systems. This is to evaluate the feasibility of using miniaturized propulsion systems in a minor body environment. The analysis examines various propulsion technologies, orbital distances, and minor bodies to assess the feasibility of flying hyperbolic arcs. Key performance metrics, including observation time, firing time, propellant consumption, and pointing accuracy, are considered.

1. Introduction

Minor body exploration is experiencing rapid growth due to various factors, including scientific, engineering, and resource utilization interests [1–3]. These bodies exhibit a wide range of sizes, shapes, and mass distributions [4,5], resulting in weak and highly non-linear dynamical fields dominated by unpredictable perturbations such as Solar Radiation Pressure (SRP). Consequently, the attitude and orbital dynamics of spacecraft in close proximity to these bodies are highly challenging and must be robust to handle diverse scenarios, as most parameters are only roughly estimated from ground-based observations [6].

Simultaneously, low-cost manufacturing and launch platforms, known as CubeSats, are increasingly being considered for missions near these bodies, as their reduced costs enable riskier operations.

Although numerous interplanetary CubeSat concepts have been studied or proposed for future missions to minor bodies [7–9], to date, only six missions, and no CubeSats, have operated in close proximity to such bodies. These missions include NEAR [10], Hayabusa-I [11], Dawn [12], Rosetta [13], Hayabusa-II [14], and OSIRIS-REx [15]. The only exception is LICIACube [16], which, however, performed a flyby of asteroid (65803) Didymos.

Two missions have been confirmed to conduct scientific investigations near asteroids. In 2027, the 6U CubeSats Milani [17] and Juventas [18] will accompany the Hera [19] platform to the asteroid (65803) Didymos to study the consequences of the DART impact [20,21]. Additionally, the RAMSES mission, scheduled for 2029, will deploy two 6U CubeSats [22] near asteroid (99942) Apophis during its close encounter with Earth. The mission aims to assess the effects of Earth's strong gravitational pull on the asteroid.

Various trajectories are possible for operations near minor bodies, with some relevant being Hyperbolic Arcs (HA), Sun-Stabilized Terminator Orbits (SSTO), and Periodic Orbits (PO). While SSTOs and POs existence and characteristics are highly dependent on the specific target body and constrained by factors such as operational range and the minor body phase angle, HAs offer greater flexibility. HAs enable operations near virtually any body at varying distances, making them an attractive choice for a wide range of mission scenarios.

Various studies have explored guidance and control methods for close proximity operations around minor bodies.

In [23], robust orbital guidance and control algorithms are developed to handle uncertainties during the approach and hovering phases of asteroids (101955) Bennu and (433) Eros, eliminating the need for extensive navigation campaigns. This work uses the cannonball model to account for SRP and targets circular trajectories, moreover the spacecraft attitude is not considered.

On the other hand, [24] simulates the approach and hovering of (101955) Bennu using autonomous navigation and orbit control. This

* Corresponding author at: Department of Aerospace Science and Technology, Politecnico di Milano, Via La Masa 34, Milan, 20156, Italy.
E-mail address: carmine.buonagura@polimi.it (C. Buonagura).

https://doi.org/10.1016/j.actaastro.2025.07.068
Received 3 March 2025; Received in revised form 14 May 2025; Accepted 30 July 2025
Available online 16 August 2025

Table 1
Relevant properties of the minor bodies considered in this work.

Body name	R_{SB} [km]	μ [km^3/s^2]	RA [deg]	Dec [deg]	Period [h]
(99942) Apophis	0.221	3.00×10^{-9}	250	−75	27.38
(101955) Bennu	0.282	4.67×10^{-9}	85.45	−60.37	4.29
67P/Churyumov–Gerasimenko	2.591	6.65×10^{-7}	69.3	64.1	12.76

study models the true SRP with a hypothetical spacecraft, assuming that its solar panels are always oriented toward the Sun. Maneuvers are represented as impulsive Δv, with the spacecraft attitude assumed to be ideal.

Additionally, [25,26] propose nonlinear landing and hovering control schemes designed for real-time onboard implementation, treating the spacecraft as a point mass.

The orbital guidance and control strategy of Milani considering the cannonball model is deeply described in [27,28]. Lastly, [29] introduces a high-fidelity 6-DOF simulator for asteroid landing scenarios, incorporating fixed propulsion system properties and utilizing reinforcement learning techniques.

Other studies that closely resemble spacecraft motion around minor bodies are those addressing the relative motion between multiple spacecraft in formation flying scenarios, due to the similarities in guidance and control strategies required in both contexts [30–32]. However, a study that accurately couples trajectory design and attitude modeling while considering a variety of propulsion systems is still missing. Given the importance of correction maneuvers and the associated attitude pointing accuracy for such operations, having such a study would be highly valuable.

In this work, we solved a guidance and control optimization problem that accurately couples attitude dynamics and trajectory design for hyperbolic proximity arcs around minor bodies, assessing the feasibility of such trajectories for different propulsion technologies and minor body properties. The most common propulsion systems for such trajectories have been considered, namely bipropellant, monopropellant, cold gas, and resistojet. Additionally, three different minor bodies are considered for analysis, specifically asteroids (99942) Apophis and (101955) Bennu, and comet 67P/Churyumov–Gerasimenko, showing a variety of size, shapes, and gravitational constant. The effects of these properties on the feasibility of HAs are evaluated, and the influence of the shape of the bodies is considered to assess its importance in the preliminary design of a space mission.

The paper is organized as follows. Section 2 provides a detailed description of the platform, the bodies involved, their trajectories, and the ConOps of the mission. In Section 3, the algorithms implemented are thoroughly described. The results of the optimization and for the different propulsion systems are presented in Section 4. Finally, conclusions are discussed in Section 5.

2. Background

In this section, the properties of the platform and the minor bodies, along with their trajectories, are described. The concept of operations for the considered mission is also outlined.

2.1. Minor bodies

Minor bodies with different gravitational constants were selected for analysis, including asteroids (99942) Apophis and (101955) Bennu, as well as comet 67P/Churyumov–Gerasimenko. These bodies were chosen because they represent a range of sizes and gravitational constants, as shown in Table 1. In this work, the selected minor bodies have distinct physical properties and characteristics but are assumed to follow the same virtual trajectory, similar to that of a Near-Earth Asteroid (NEA), whose orbital elements are listed in Table 2.

The main assumption considered is that the minor body is at its minimum distance from the Sun, approximately 0.65 AU, and that the Earth is positioned along its orbit at the point of minimum distance from the minor body. This orbital configuration enables testing the feasibility of hyperbolic trajectories under the most challenging conditions, where SRP and the third-body perturbations from the Sun and Earth are particularly significant. The assumption that the Sun–minor body vector remains constant is justified due to the short mission duration considered in our analyses.

Table 2
Minor body trajectory orbital elements.

a [AU]	e [–]	i [deg]	Ω [deg]	ω [deg]
1.47	0.56	6.35	35.5	286

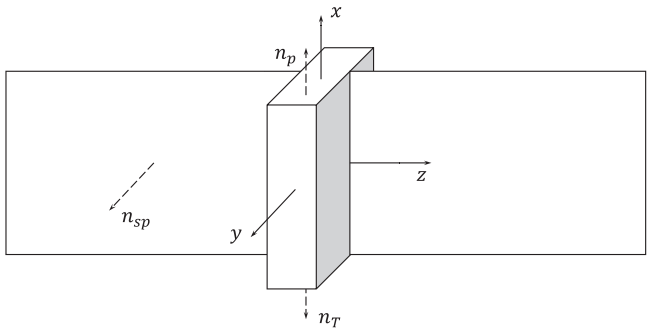

Fig. 1. Schematic representation of the 6U platform. n_p, n_{sp}, and n_T represent the normal vectors of the payload, solar panels, and thruster, respectively.

2.2. Platform

The platform considered in this work is a 6U CubeSat, identical to the one proposed for the Milani mission [28]. Considering the CubeSat body-fixed frame, the scientific payload is assumed to point along the positive x-axis, while the main propulsion system is located on the same axis but on the opposite face of the spacecraft. The solar panels are aligned with the z-axis, with their normal oriented toward the positive y-axis. These panels are fixed in this configuration, as there is no mechanism to allow their rotation. It is also assumed that the spacecraft center of mass (CoM) is displaced from the platform geometric center by an amount modeled as zero-mean white Gaussian noise.

$$\Delta \mathbf{r}_{CoM} = N(0, \Delta r^2_{CoM,max}/9) \quad \text{where} \quad \Delta r_{CoM,max} = 1.5\,\text{cm} \tag{1}$$

A CubeSat schematic representation, along with the body reference frame, and relevant normal vectors are reported in Fig. 1.

The CubeSat mass m_{SC} is 12 kg, including 1 kg of propellant mass m_{prop}. An equivalent reflectivity coefficient $C_r = 1.24$ is considered.

The CubeSat will fly hyperbolic trajectories in the vicinity of the minor bodies. Specifically, the minimum distance of the trajectory key points from the body center of mass is set to $3R_{SB}$ where R_{SB} represents the equivalent radius of the body. The maximum distance is set to $1.2r_{SOI}$, where r_{SOI} is the radius of the Sphere of Influence (SOI) of the considered body.

$$r_{SOI} = r_{B-S}\left(\frac{m_A}{m_S}\right)^{2/5} \tag{2}$$

where r_{B-S} is the distance of the minor body from the Sun, and m_A and m_S (1.9891×10^{30} kg) are the masses of the body and the

Fig. 2. Schematic representation of the spacecraft concept of operations.

Sun, respectively. These limiting distances have been chosen for safety reasons to mitigate the risks of impact and escape from the body.

2.3. Concept of operations

The mission concept of operation alternates between phases of small body pointing for scientific observations, and slew and firing phases required to follow the desired attitude and hyperbolic trajectory.

Firstly, the CubeSat is deployed from a mothercraft in a low-altitude orbit. After de-tumbling, the spacecraft aligns with the desired attitude for firing. This phase can be referred as commissioning. Our simulations begin at this point, assuming that the spacecraft is already aligned to the desired attitude configuration.

The CubeSat then starts firing at maximum thrust to achieve injection into a hyperbolic trajectory. During this phase, the control actuators must ensure the correct attitude for thrusting, following the desired thruster azimuth and elevation angles. Once firing is completed, the Attitude Determination and Control System (ADCS) commands the spacecraft to switch to minor body pointing mode. A slew maneuver is performed to transition from thrusting mode to small body pointing mode. After this phase, the spacecraft payload is aligned with the small body–spacecraft vector, and the attitude is adjusted to maximize incoming solar power by minimizing the angle between the solar panels normal and the Sun direction vector. During this phase, the spacecraft points toward the small body center of mass to conduct scientific observations, and the actuators must ensure the correct attitude for both small body pointing and solar power maximization. Following this, the ADCS commands the spacecraft to switch back to firing mode, and a slew maneuver is performed to transition to this mode. Once the thrust direction is achieved, the CubeSat starts firing at maximum thrust to be injected into the successive hyperbolic trajectory. The control actuators must ensure the correct attitude for thrusting. This process is repeated until the end of the mission, depending on the available onboard propellant and mission requirements. The time allocated for performing slew maneuvers has been fixed at 10 min for the analyses. A schematic representation of the spacecraft ConOps is show in Fig. 2.

3. Methodology

In this work, we conducted simulations of CubeSat close proximity operations around minor bodies following hyperbolic trajectories, utilizing a variety of commonly used propulsion systems for such platforms. The 6-DoF simulations couple attitude dynamics with trajectory design, enabling the assessment of how the spacecraft attitude evolution influences the guidance strategy used to target key points around the minor body.

3.1. Equations of motion

The dynamical models presented in this work encompass both orbital dynamics and attitude dynamics and kinematics, taking into account the effects of mass evolution due to spacecraft maneuvers.

Orbital dynamics. The spacecraft orbital dynamics in the vicinity of low-gravity bodies such as asteroids and comets is highly nonlinear and influenced by perturbations such as SRP and third-body effects. Specifically, considering a J2000 inertial frame centered at the minor body center of mass, the acceleration experienced by the CubeSat can be divided into various contributions, expressed in this frame:

$$\ddot{\mathbf{r}} = \mathbf{a}_b + \mathbf{a}_{SRP} + \mathbf{a}_{3b,s} + \mathbf{a}_{3b,p} + \mathbf{a}_T \tag{3}$$

where $\mathbf{a}_b$ represents the acceleration due to the small body, computed using the point mass model, as it is assumed that the CubeSat remains outside the minor body Brillouin sphere

$$\mathbf{a}_b = -\frac{\mu}{r^3}\mathbf{r} \tag{4}$$

where μ is the gravitational parameter of the minor body, and $\mathbf{r}$ and r represent the position and distance of the spacecraft relative to the body center of mass, respectively.

The acceleration due to SRP is denoted as $\mathbf{a}_{SRP}$, calculated as the sum of the contributions from each CubeSat face illuminated by the Sun.

$$\mathbf{a}_{SRP} = \begin{cases} A_{BN} \sum_{i=1}^{10} \frac{P_0}{c} \left(\frac{D_{AU}}{r_{C-S,B}} \right)^2 \frac{C_r A_i (-\hat{\mathbf{r}}_{C-S,B} \cdot \mathbf{n}_i)}{m_{SC}} \hat{\mathbf{r}}_{C-S,B} & \text{if} \quad -\hat{\mathbf{r}}_{C-S,B} \cdot \mathbf{n}_i > 0 \\ \mathbf{0} & \text{if} \quad -\hat{\mathbf{r}}_{C-S,B} \cdot \mathbf{n}_i \leq 0 \end{cases} \tag{5}$$

where P_0 ($1367\,\mathrm{W/m^2}$) is the solar flux at 1 AU, c is the speed of light (2.998×10^8 m/s), D_{AU} is the Sun–Earth distance (1 AU), and A_i and n_i are the ith surface area of the platform and its normal vector, respectively. $\mathbf{r}_{C-S}$ is the position vector of the field point with respect to the Sun. The SRP is then computed in the inertial frame by rotating its value from the spacecraft body-fixed frame using the rotation matrix A_{BN}.

The third-body perturbations from the Sun and Earth are computed as

$$\mathbf{a}_{3b,pb} = (\mu_{pb} + \mu)\frac{\mathbf{r}_{b-pb}}{r_{b-pb}^3} - \mu_{pb}\frac{\mathbf{r}_{C-pb}}{r_{C-pb}^3} \tag{6}$$

where the subscript pb refers to the perturbing body, meaning the numerical values will differ depending on whether the Sun or Earth is considered. Specifically, μ_{pb} is the gravitational parameter of the perturbing body, while r_{b-pb} and r_{C-pb} are the position vectors of the minor body barycenter and the field point relative to the perturbing body, expressed in the minor body inertial frame.

Finally $\mathbf{a}_T$ represents the acceleration due to the spacecraft control actions, specifically provided by its main propulsion system. Its value can be computed as

$$\mathbf{a}_{T,B} = -A_{BN} T \frac{\mathbf{n}_T}{m_{SC}} \tag{7}$$

where T is the thrust generated by the spacecraft, and $\mathbf{n}_T$ is the normal vector of the face where the propulsion system is mounted. The resulting acceleration, computed in the body-fixed frame, is then rotated into the inertial frame using the A_{BN} rotation matrix. The attitude profile is expressed in terms of two angles: azimuth Az and elevation El. These angles are parametrized in time as third-order polynomial functions [33].

$$Az(t) = a_1 + a_2 t + \frac{a_3}{2}t^2 + \frac{a_4}{6}t^3 \quad \text{where} \quad \mathbf{a}_m = [a_1, a_2, a_3, a_4]^T \tag{8}$$

$$El(t) = b_1 + b_2 t + \frac{b_3}{2}t^2 + \frac{b_4}{6}t^3 \quad \text{where} \quad \mathbf{b}_m = [b_1,\, b_2,\, b_3,\, b_4]^T \tag{9}$$

The firing direction vector $\mathbf{n}_T(t)$ is then computed as

$$\mathbf{n}_T(t) = [\cos Az(t)\cos El(t),\ \sin Az(t)\sin El(t), \sin El(t)]^T \tag{10}$$

Attitude dynamics and kinematics. The spacecraft attitude, represented as a quaternion, is propagated using the spacecraft kinematic equation

$$\dot{\mathbf{q}} = \frac{1}{2}\Omega(\boldsymbol{\omega})\mathbf{q} \tag{11}$$

Where $\boldsymbol{\omega}$ is the spacecraft angular rate, and $\mathbf{q}$ is the spacecraft attitude quaternion, consisting of a vector part $\bar{v}$ and a scalar part s.

$$\mathbf{q} = \begin{bmatrix} s \\ \bar{\mathbf{v}} \end{bmatrix}; \quad s \in \mathbb{R}^1 \quad \bar{\mathbf{v}} \in \mathbb{R}^3; \tag{12}$$

The matrix $\Omega(\boldsymbol{\omega})$ is defined as:

$$\Omega(\boldsymbol{\omega}) = \begin{bmatrix} 0 & -\boldsymbol{\omega}^T \\ \boldsymbol{\omega} & -\boldsymbol{\omega}^{\times} \end{bmatrix} \tag{13}$$

where $[\cdot]^{\times}$ is the skew-symmetric or cross-product matrix.

The kinematic equation is coupled with the dynamics equation to retrieve the spacecraft angular rate.

$$J\dot{\boldsymbol{\omega}} = J\boldsymbol{\omega} \times \boldsymbol{\omega} + \boldsymbol{\tau} + \mathbf{u}_c \tag{14}$$

where J is the spacecraft inertia matrix, τ represents the external torques acting on the spacecraft, and $\mathbf{u}_c$ denotes the attitude control input. The external torque τ considered is induced by the SRP due to the displacement between the spacecraft center of mass and its geometric center. Specifically, it is computed as:

$$\tau = A_{BN} \sum_{i=1}^{10} \mathbf{f}_i \times \mathbf{a}_{SRP,B} m_{SC} \tag{15}$$

where $\mathbf{f}_i$ is the position of the center of the ith surface relative to the spacecraft CoM. While the attitude control consists of two terms, the gyroscopic effect feedforward compensation and the control authority $\mathbf{u}_a$

$$\mathbf{u}_c = \boldsymbol{\omega} \times J\boldsymbol{\omega} + \mathbf{u}_a \tag{16}$$

The control authority is implemented as a proportional–derivative (PD) control action, constrained by the maximum torque achievable by actuators on a 6U CubeSat.[1]

$$\mathbf{u}_a = -K_d \Delta\boldsymbol{\omega} - K_p \Delta\boldsymbol{\theta} \quad \text{with} \quad |\mathbf{u}_a| < 0.007 I \,\text{N m} \tag{17}$$

where $\Delta\boldsymbol{\omega}$ and $\Delta\boldsymbol{\theta}$ are the angular velocity and attitude errors, calculated as the differences between the actual and desired values, and I is the 3 × 3 identity matrix. The gain matrices K_p and K_d are selected through a trial-and-error approach based on the phase of the mission, with different values considered for the firing, cruising, and slew phases, as detailed in Table 3. While optimizing the selected gains to account for the varying moments of inertia along the spacecraft principal axes could yield more refined results, the present study focuses on demonstrating the feasibility and effectiveness of the proposed control strategy using a non-optimized set of gains.

Mass dynamics. The spacecraft mass shows an evolution only during the firing phase, when the thruster is active. During this phase, the mass can be propagated using the relation

$$\dot{m} = -\frac{T}{I_{sp} g_0} \tag{18}$$

where I_{sp} is the spacecraft specific impulse, and g_0 (9.81 m/s^2) is the standard gravitational acceleration at Earth's surface.

[1] CD-DEV.PD.CW-01, CubeWheel Gen 2 Product Description, Ver.1.01, https://www.cubespace.co.za/uploads/7007f7f5-f682-49d6-94d3-13d2cf3c5a93.pdf, Last accessed: December 20, 2024.

Table 3
Attitude control gains for the different simulation phases.

Mission phase	K_p [N m]	K_d [N m s]
Cruising	$3 \times 10^{-4} I$	$1 \times 10^{-2} I$
Firing	$30 I$	$7 \times 10^{-2} I$
Slew	$3 \times 10^{-3} I$	$7.75 \times 10^{-2} I$

3.2. Statement of the problem

The final objective of this work is to assess the feasibility of hyperbolic trajectories close to minor bodies by minimizing the amount of propellant consumed along the trajectory. To achieve this, an optimization problem is formulated as a Nonlinear Programming (NLP) problem. The vector of optimization variables $\mathbf{y}$ is as follows

$$\mathbf{y} = [T_1,\, T_2,\, \Delta t_1,\, \Delta t_2^1,\, \Delta t_2^2,\, \mathbf{a}_m^1,\, \mathbf{b}_m^1,\, \mathbf{a}_m^2,\, \mathbf{b}_m^2,\, \mathbf{x}_k,\, m_f]^T \tag{19}$$

where T_1 and T_2 are the time instants of the second and third key points, respectively, Δt_1, Δt_2^1, and Δt_2^2 are the time durations of the first and second firings. It is important to note that the second maneuver is divided in two intervals, centered at T_1, to allow the optimizer to achieve an asymmetric firing before and after the second key point. As described in Eq. (9), $\mathbf{a}_m^1$, $\mathbf{b}_m^1$, $\mathbf{a}_m^2$, and $\mathbf{b}_m^2$ are the vectors of cubic polynomial coefficients describing the evolution of the azimuth Az and elevation El angles during both firings. The spacecraft states (position and velocity) at specific selected points along the trajectory are indicated as $\mathbf{x}_k$, and m_f is the final mass of the spacecraft.

The objective function $f(\mathbf{y})$, as mentioned above, is given by

$$f(\mathbf{y}) = -m_f \tag{20}$$

Minimizing the negative of the final mass m_f is equivalent to maximizing the final spacecraft mass, thereby minimizing propellant consumption.

This problem must be solved subject to a set of constraints. Firstly, initial conditions constraint can be defined, where the initial state and time are fixed to prescribed values: the starting time of the simulation and the first key point of the hyperbolic trajectory, respectively. The attitude is also constrained throughout the entire duration of the simulation to follow a desired attitude profile. These conditions can be summarized as

$$t_0 = t_0^* \tag{21}$$

$$\mathbf{x}_0 = \mathbf{x}_0^* \tag{22}$$

$$\mathbf{q}(t) = \mathbf{q}^*(t) \tag{23}$$

The desired attitude $\mathbf{q}^*$ is a function of the mission phase (firing, small-body pointing, slew), and will be discussed in Section 3.3.

A set of nonlinear inequality and equality constraints can also be defined. Specifically, with regard to the inequality constraints, it is imposed that the spacecraft must be inside a spatial cube when at the time instants of the second and third key points of the nominal hyperbolic trajectory, and the final eccentricity of the trajectory must be greater than 1.2. This eccentricity condition has been introduced as a safety margin to mitigate the risk of impact with the small body [27]. These conditions are expressed as

$$\mathbf{r}(T_1) \in C_1 \tag{24}$$

$$\mathbf{r}(T_2) \in C_2 \tag{25}$$

$$e(T_2) > 1.2 \tag{26}$$

where C_1 and C_2 represent two cubic regions, the extent of which depends on the distance of the key points from the minor body. Specifically, the size of their edges is equal to

$$l_C = 0.10 d_{SC-SB} \tag{27}$$

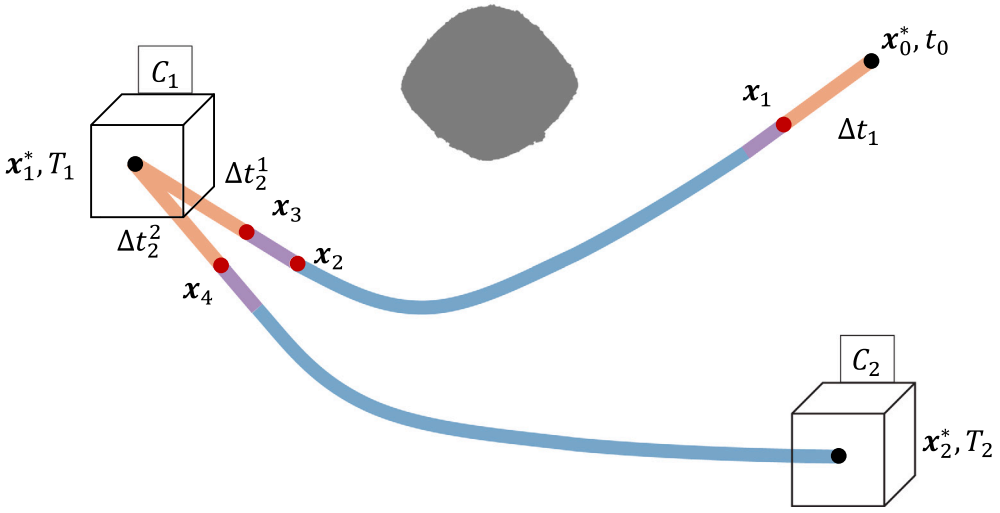

Fig. 3. Schematic representation of the hyperbolic trajectory considered along with some relevant parameters.

These regions have been assumed to be cubic to simplify the definition of constraints in the optimization. The nonlinear equality constraints depend on the multiple shooting algorithm [34] that has been implemented. Their goal is to minimize the position and velocity defects at each multiple shooting point and can be expressed as

$$\mathbf{x}(t) = \phi(\mathbf{x}_k, t_k, t_{k+1}) \quad \text{with} \quad k = 0, \dots, m-1 \tag{28}$$

were m is the number of multiple shooting points. In this analysis, we consider $m = 4$. Specifically, these points are at the end of the first firing, before the slew maneuver from minor body pointing to firing, and before and after the second firing.

Lower bounds are set for the firing durations, corresponding to a value of 0.5 s.

Finally, the NLP problem can be formulated as follows

$$\min_{\mathbf{y}} f(\mathbf{y}) \quad \text{s.t.} \quad \begin{cases} t_0 = t_0^* \\ \mathbf{x}_0 = \mathbf{x}_0^* \\ \mathbf{q}(t) = \mathbf{q}^*(t) \\ \mathbf{r}(T_1) \in C_1 \\ \mathbf{r}(T_2) \in C_2 \\ e(T_2) > 1.2 \\ \mathbf{x}(t) = \phi(\mathbf{x_k}, t_k, t_{k+1}) \quad \text{with} \quad k = 0, \dots, m-1 \end{cases} \tag{29}$$

$$\Delta t_1 \in [0.50, \infty] \tag{30}$$

$$\Delta t_2^1 \in [0.25, \infty] \tag{31}$$

$$\Delta t_2^2 \in [0.25, \infty] \tag{32}$$

A schematic trajectory with all the important parameters is shown in Fig. 3.

3.3. First guess generation

The first guess for the optimization problem is constructed following a three-step procedure.

Impulsive trajectory. In the first step, considering only the point mass gravity of the small body and given two random points at a fixed distance from the body, a Lambert problem [35] is solved to determine the $\Delta v_{Lambert}$ required to transfer from one point to the other. Since there are multiple solutions depending on the time of flight, a zero-finding problem is solved to ensure that the trajectory eccentricity is equal to 1.2.

The second step involves incorporating all the perturbations present in the considered dynamical environment, as shown in Eq. (3). A simple shooting method is then applied to compute the initial spacecraft velocity, allowing the final propagated position to match the desired target point. Once the distance between the propagated position and the target one is below a certain tolerance, the problem is solved and the new impulsive maneuver Δv_{ss} is found.

Maneuver spreading. At this point, as a third step, it is necessary to spread the impulsive maneuvers along the trajectory to properly simulate the propulsion system and the attitude evolution during firing. To do so, a constant attitude profile is considered for the generation of the first guess, and the firing time duration is computed based on the propulsion system properties.

$$\Delta t_{firing} = \frac{m_{SC} \Delta v_{ss}}{T} \tag{33}$$

Desired attitude computation. The desired attitude varies across the three phases of the mission, and must be computed accordingly.

For the firing phase, the desired attitude depends on the thruster direction vector γ. Given that the thruster direction is along the x-axis in the spacecraft body frame, an eigen-axis, eigen-angle rotation can be used to compute the body-to-inertial frame rotation matrix required for the spacecraft attitude control. The desired angular velocity is set to the null vector.

For the small-body pointing phase, the desired rotation matrix is built to align the x-axis with the small body and minimize the angle between the solar panel normals and the Sun direction. This attitude will be referred to as power maximization (PM).

$$A_B^{PM} = \begin{bmatrix} \hat{i} = -\hat{r} \\ \hat{j} = \frac{\hat{k} \times \hat{i}}{\|\hat{k} \times \hat{i}\|} \\ \hat{k} = \frac{\hat{r} \times \hat{r}_{C-S,B}}{\|\hat{r} \times \hat{r}_{C-S,B}\|} \end{bmatrix}^T \tag{34}$$

In the specific case where the unit vectors $\hat{r}$ and $\hat{r}_{C-S,B}$ are aligned, the rotation matrix is reinitialized to match that of the previous time step. However, it must be remarked that this condition did not arise in any of the simulations performed.

The desired quaternion representation can then be computed easily. In this phase, the desired angular velocity is also determined. The angular velocity in the local vertical local horizontal (LVLH) frame is computed considering a magnitude of $\omega = v/r$ and a direction aligned and opposite to the orbital angular momentum vector. The rotation matrix from the body frame to the LVLH frame is given by

$$A_B^{LVLH} = \begin{bmatrix} \hat{i} = -\hat{r} \\ \hat{j} = \frac{\hat{k} \times \hat{i}}{\|\hat{k} \times \hat{i}\|} \\ \hat{k} = -\frac{\hat{r} \times \hat{v}}{\|\hat{r} \times \hat{v}\|} \end{bmatrix}^T \tag{35}$$

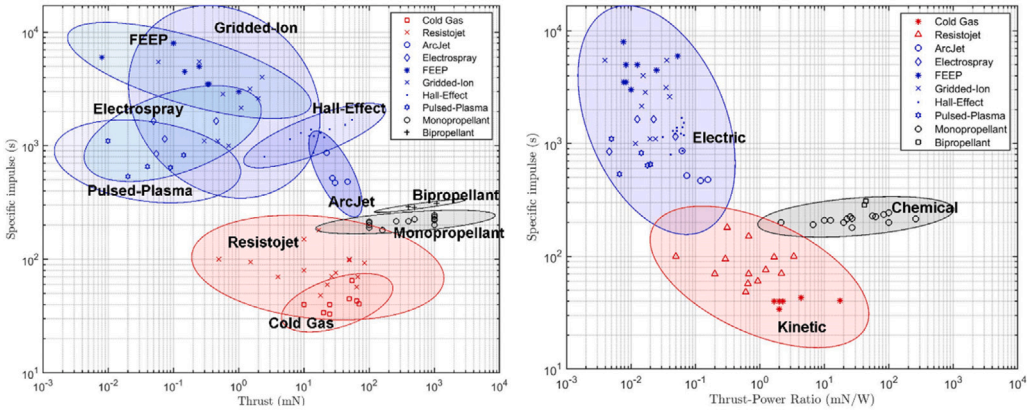

Fig. 4. Propulsion system review for miniaturized platforms [36].

The rotation matrix from LVLH to the PM frame is defined as

$$A_{LVLH}^{PM} = A_B^{PM}[A_B^{LVLH}]^T \tag{36}$$

this can then be used to compute the angular velocity in the desired reference frame.

For the slew phase, an eigenaxis rotation slew maneuver is considered, which is a controlled rest-to-rest motion between two attitudes. The final desired attitude is either the firing mode or the minor body pointing mode, and the desired angular velocity is set to the null vector.

The orthonormality of all the computed rotation matrices is ensured by verifying that

$$[A_i^j]^T A_i^j = I \tag{37}$$

3.4. Propulsion systems selection

There is a wide spectrum of miniaturized propulsion systems tailored for CubeSats. Three broad categories can be distinguished: chemical, kinetic, and electrical [36]. In this analysis, electrical thrusters are not considered due to their limited thrust over power capabilities, which are not suitable for hyperbolic arcs. Chemical propulsion can be divided into bipropellant and monopropellant systems, while kinetic propulsion includes cold gas and resistojet systems. Regarding the resistojet, it is important to consider the amount of power available to the propulsion system. Assuming 100 W as the power available for the subsystem, the average Thrust-to-Power ratio required for the specific technology can be computed from Fig. 4(b). Consequently, the maximum thrust achievable with these systems, given the available power, can be determined. Specifically, for the resistojet, the maximum thrust achievable is 150 mN. The other propulsion systems considered are not significantly affected by the incoming power and for this reason a maximum thrust of 1 N is assumed to be a plausible value for miniaturized platforms like CubeSats. The range of specific impulses has been computed from the range of thrusts shown in Fig. 4(a). However, to simplify the search space, the specific impulse has been fixed at the maximum value within the computed range.

The properties of the propulsion systems considered in this work are reported in Table 4.

3.5. Analyses performed

Two analyses were conducted to test the performance and robustness of propulsion systems in the proximity of minor bodies.

Table 4
Selected propulsion systems properties.

Propulsion system	T_{range} [mN]	$T_{average}$ [mN]	$I_{sp,range}$ [s]	I_{sp} [s]
Bipropellant	100–1000	550	250–350	350
Monopropellant	20–1000	510	150–250	250
Cold gas	5–200	102.5	40–80	80
Resistojet	0.5–150	75.25	20–150	150

Variable thrust. The key points of the hyperbolic trajectories were chosen to be at an average distance from the minor body, specifically

$$D_{kp} = \frac{D_{min} + D_{max}}{2} \tag{38}$$

The analysis was carried out considering the different propulsion systems, spanning the range of thrusts, to assess the feasibility of the trajectory and the minimum possible thrust required to fly these arcs.

Variable distance. The thrust values for each propulsion system were fixed at the average value within the range of thrusts considered, and the distance from the minor body was allowed to vary from D_{min} to D_{max}. Specifically, ten different trajectories were considered for this analysis.

3.6. Performance metrics

It is required to define some metrics to assess the performance of the propulsion systems and control methods employed in our simulations. Four metrics have been defined, which will be further discussed below.

- **Observation time percentage**. It is the percentage of time along the trajectory when the spacecraft is pointing toward the minor body and scientific observations can be conducted. The condition that must be satisfied is

$$\hat{\gamma}(t) \cdot -\hat{r}(t) \geq 1 + \epsilon \tag{39}$$

where ϵ is a tolerance value depending on the desired pointing accuracy we want to achieve, 2 deg for our simulations.
The observation time can then be computed as

$$T_{obs} = \sum_{k=0}^{n} H[(\hat{\gamma}(t) \cdot -\hat{r}(t)) - (1+\epsilon)](t_{k+1} - t_k) \tag{40}$$

where H is the Heaviside function. Consequently, the observation time percentage can be computed as

$$\eta_{obs} = \frac{T_{obs}}{T_2} \cdot 100 \tag{41}$$

- **Firing time**. This metric is the total firing time during the mission and can be computed as

$$\Delta t_{firing} = \Delta t_1 + \underbrace{\Delta t_2^1 + \Delta t_2^2}_{\Delta t_2} \tag{42}$$

- **Percentage of propellant consumed**. The consumed mass of propellant can be computed from the firing time Δt_{firing} as

$$m_{consumed} = \frac{T}{I_{sp} g_0} \Delta t_{firing} \tag{43}$$

Consequently, the percentage of propellant consumed is

$$m_p = \frac{m_{consumed}}{m_{prop}} \cdot 100 \tag{44}$$

- **Pointing accuracy**. This metric is used to assess the performance of the attitude control system. It is specifically evaluated during the minor body pointing phase, when precise pointing of the payload toward the minor body is required. The pointing accuracy δ_{point} is computed from the attitude error expressed in terms of quaternions.

$$\Delta \mathbf{q}(t) = \begin{bmatrix} \Delta \mathbf{q}_s(t) \\ \Delta \mathbf{q}_v(t) \end{bmatrix} = \mathbf{q}(t) \otimes \mathbf{q}_d(t) \tag{45}$$

where $\otimes$ represents the quaternion product, $\mathbf{q}$ is the true spacecraft attitude, and $\mathbf{q}_d$ is the desired quaternion at time t. The pointing accuracy is then determined as the norm of the vector part of the quaternion error.

$$\delta_{point} = \max \|\Delta \mathbf{q}_v\| \tag{46}$$

4. Results

In this section, simulation results of the optimization algorithm are presented to demonstrate that all propulsion systems are compatible with miniaturized platforms such as CubeSats. Additionally, numerical results from the analyses of variable thrust and variable distance are provided for the three bodies considered. A final comparison and the effects of high-fidelity gravitational models are also presented.

4.1. Optimization

Since numerous simulations were conducted with various bodies, propulsion systems, and orbital distances, only one representative case will be described to illustrate the optimization results. The findings for other cases showed no significant deviations in trends across various bodies, distances, and thrust levels. In this representative scenario, the minor body considered is (99942) Apophis, and the platform is equipped with a cold gas thruster producing a thrust of 8 mN. The trajectory analyzed corresponds to the one at average distance.

The final trajectory, along with the attitude profile and the impulsive thrust directions of the initial guess, is shown in Fig. 5(a). Fig. 5(b) illustrates the propellant mass evolution throughout the simulation. It is evident that the mass decreases only during thrust firings. The firing attitude profile is calculated to ensure that all optimization constraints are satisfied while maximizing the final spacecraft mass. The duration of the maneuvers plays a crucial role in the evolution of the attitude. For impulsive technologies, this time interval is reduced to just a few seconds, leading to a nearly constant attitude during firing. Two examples of attitude angles for the minimum and maximum thrust levels considered for a cold gas thruster are shown in Fig. 6.

The evolution of key spacecraft parameters along the trajectory is presented in Figs. 7 and 8. These figures include inset plots highlighting the slew and firing phases, where parameter variations are more pronounced compared to nominal operation phases (e.g., minor body pointing).

To validate the spacecraft attitude control performance, Fig. 7 illustrates the attitude and angular velocity errors relative to the desired values.

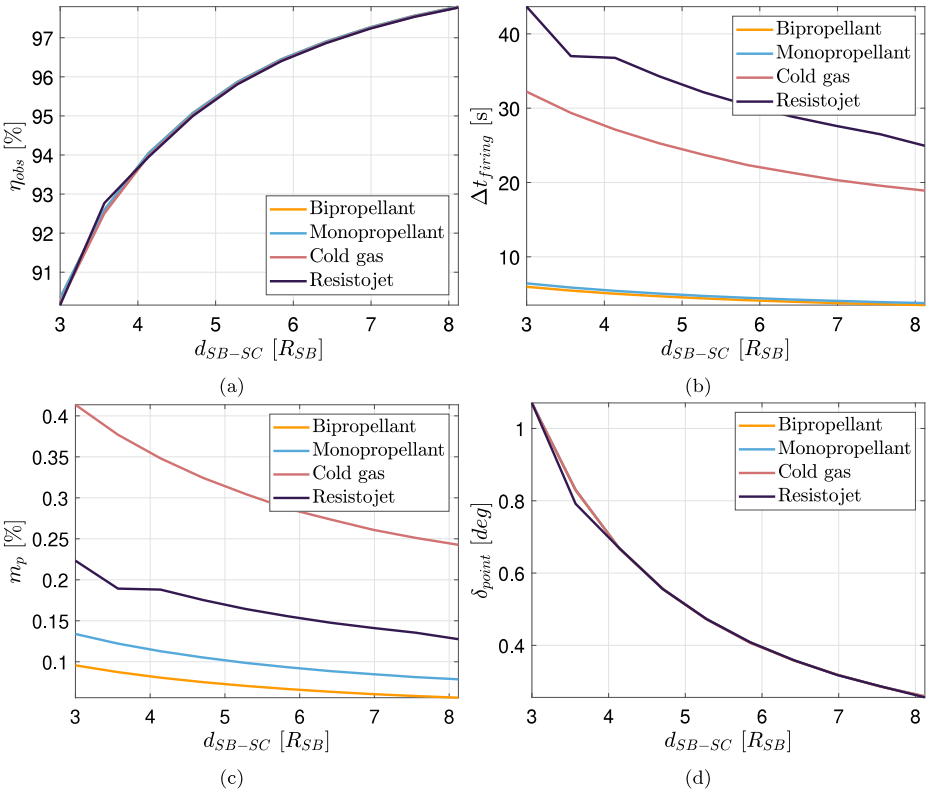

Fig. 5. (a) Optimized spacecraft orbital and attitude profiles, and (b) mass evolution throughout the simulation.

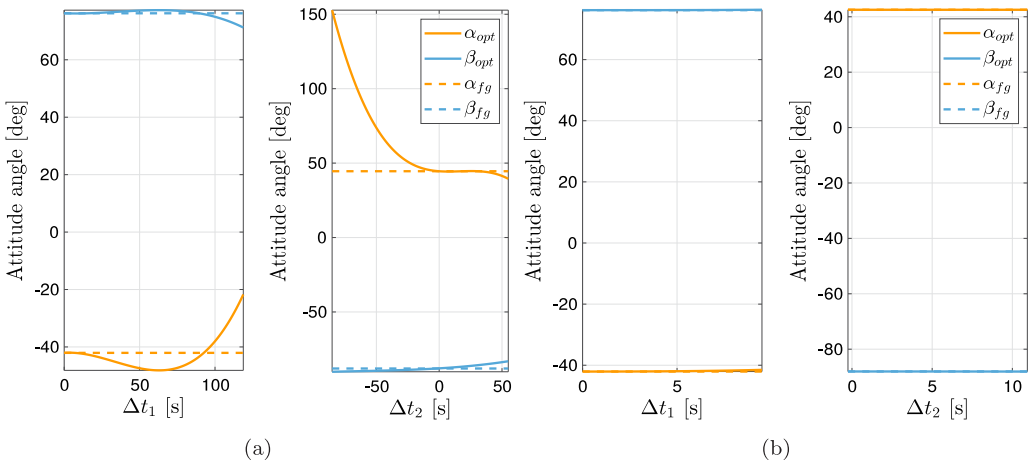

Fig. 6. Spacecraft attitude profile in terms of azimuth and elevation for (a) an 8 mN cold gas thruster and (b) a 200 mN cold gas thruster.

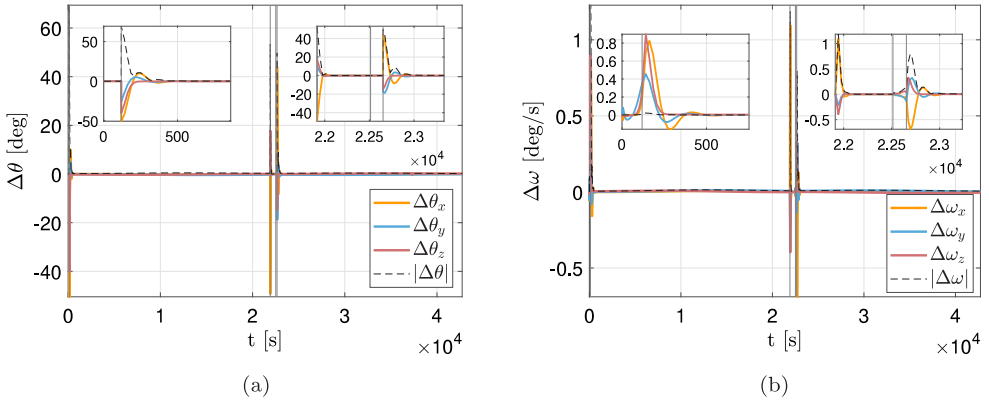

Fig. 7. Spacecraft (a) attitude and (b) angular velocity errors throughout the simulation. The inset plots, show the components evolution during firing and slew phases.

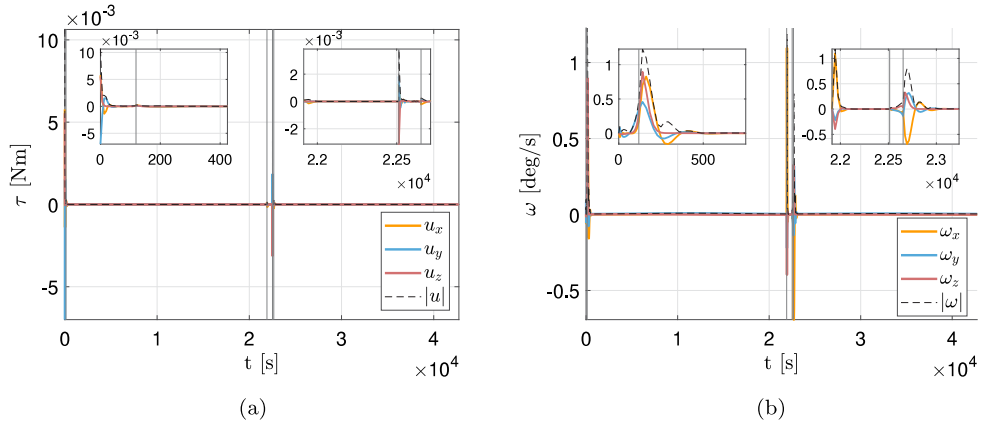

Fig. 8. (a) Actuators control action (b) and spacecraft angular velocity throughout the duration of the simulation. The inset plots show the components evolution during firing and slew phases.

The attitude error is calculated as the angular deviation along each spacecraft axis, obtained by converting the quaternion representation to angular coordinates. From the plots, it is evident that the largest errors occur during slew maneuvers, with maximum angular and angular velocity errors of 60 deg and 1 deg/s, respectively. Both images also indicate that the attitude control settling time remains below 500 s, which is well within the 10 min time slot allocated for slew maneuvers.

Additionally, the control torque is constrained by technological limitations to 0.007 N m per axis. Fig. 8(a) shows that the maximum control action consistently remains below this threshold, with slight peaks observed during slew phases, while Fig. 8(b) shows the angular velocity evolution.

4.2. Variable thrust

The variable thrust analysis was conducted for the three bodies under consideration. While the firing time exhibits a clear trend as thrust values increase, the other metrics remain largely consistent across the range of thrust values. For this reason, the firing time trends are graphically illustrated in Figs. 9, 10, and 11 for (99942) Apophis,

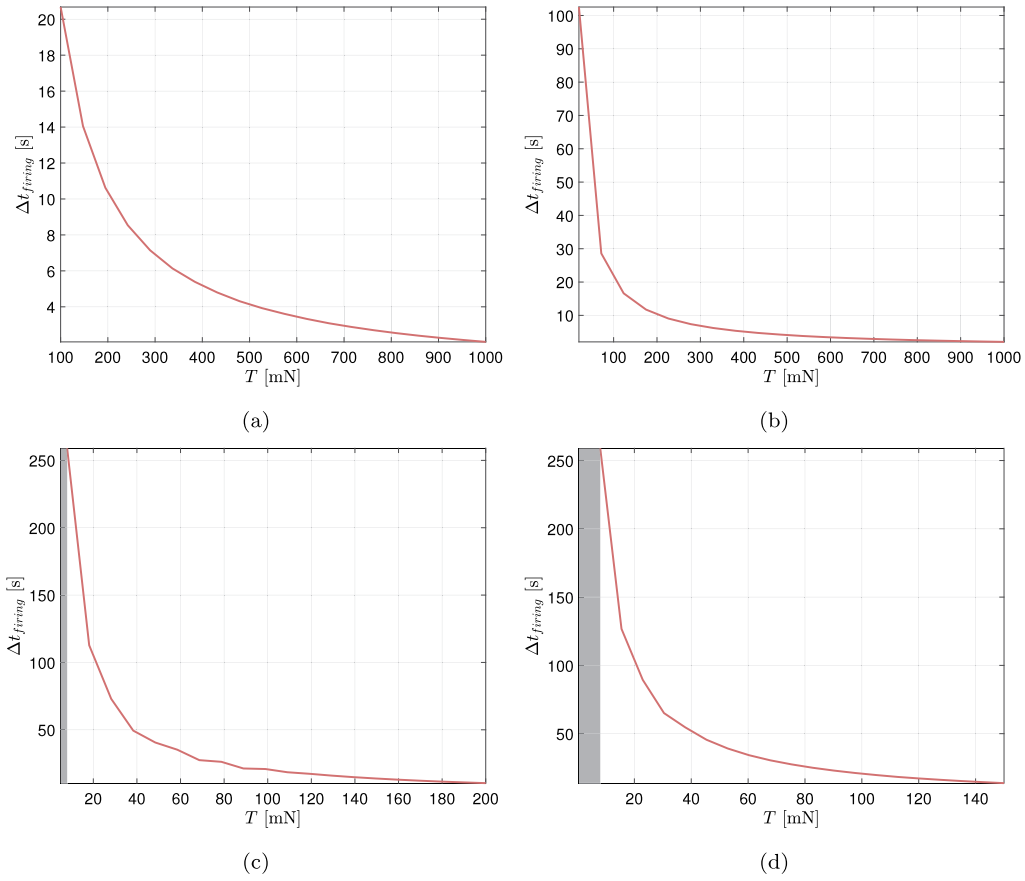

Fig. 9. Variable thrust analysis for asteroid (99942) Apophis considering different propulsion systems, namely (a) bipropellant, (b) monopropellant, (c) cold gas, and (d) resistojet.

Table 5
Maximum and minimum performance metrics for variable thrust analysis of asteroid (99942) Apophis.

Thruster	η_{obs}^{max} [%]	η_{obs}^{min} [%]	m_p^{max} [%]	m_p^{min} [%]	δ_{point}^{max} [deg]	δ_{point}^{min} [deg]
Bipropellant	95.73	95.69	0.0603	0.0597	0.4990	0.4847
Monopropellant	95.73	95.50	0.0836	0.0831	0.5075	0.4994
Cold gas	95.85	95.15	0.2651	0.2401	0.4904	0.4583
Resistojet	95.71	95.15	0.1408	0.1333	0.4850	0.4716

Table 6
Maximum and minimum performance metrics for variable thrust analysis of asteroid (101955) Bennu.

Thruster	η_{obs}^{max} [%]	η_{obs}^{min} [%]	m_p^{max} [%]	m_p^{min} [%]	δ_{point}^{max} [deg]	δ_{point}^{min} [deg]
Bipropellant	96.17	96.13	0.0691	0.0685	0.4418	0.4317
Monopropellant	96.17	95.96	0.0972	0.0965	0.4359	0.4279
Cold gas	96.26	95.69	0.2972	0.2725	0.4465	0.4200
Resistojet	96.25	95.70	0.1593	0.1456	0.4510	0.4211

(101955) Bennu, and 67P/Churyumov–Gerasimenko, respectively. Additionally, the maximum and minimum values of the other metrics for the different thrusters are summarized in Tables 5, 6, and 7.

As expected, the firing time decreases monotonically with increasing thrust values. However, certain thrust values do not allow for feasible hyperbolic trajectories; these cases are indicated by a gray area in the figures. Despite the varying firing times for the analyzed bodies, the minimum thrust value required for feasible trajectories differs. Specifically, it is 8 mN for (99942) Apophis, 10 mN for (101955) Bennu, and 60 mN for comet 67P/Churyumov–Gerasimenko. This topic will be discussed further in Section 4.4.

Table 7
Maximum and minimum performance metrics for variable thrust analysis of comet 67P/Churyumov–Gerasimenko.

Thruster	η_{obs}^{max} [%]	η_{obs}^{min} [%]	m_p^{max} [%]	m_p^{min} [%]	δ_{point}^{max} [deg]	δ_{point}^{min} [deg]
Bipropellant	97.69	97.52	0.3053	0.2777	0.2863	0.2672
Monopropellant	97.71	97.46	0.4295	0.3860	0.2778	0.2575
Cold gas	97.67	97.47	1.2163	1.1879	0.2656	0.2562
Resistojet	97.65	97.54	0.6633	0.6440	0.2668	0.2548

4.3. Variable distance

The same bodies are analyzed with trajectories at varying distances from the body surface. The observation time percentage, firing time, propellant consumption, and pointing accuracy are reported for each propulsion system, with thrust held constant and equal to the average value.

As the distance from the minor body increases, the observation time percentage increases consistently across all propulsion systems.

In contrast, the firing time decreases with increasing distance, with the effect being more significant for technologies with lower thrust. As a result, the resistojet exhibits the highest firing times at all distances, while the bipropellant and monopropellant systems overlap due to their similar thrust values.

The propellant consumption follows the same trend as the firing time and is primarily driven by the specific impulse: the lower the specific impulse, the higher the propellant consumption. Consequently, the cold gas thruster exhibits the highest propellant consumption, while the bipropellant system demonstrates the lowest.

Finally, the pointing accuracy decreases as the distance from the minor body increases. This is because the trajectory evolves more

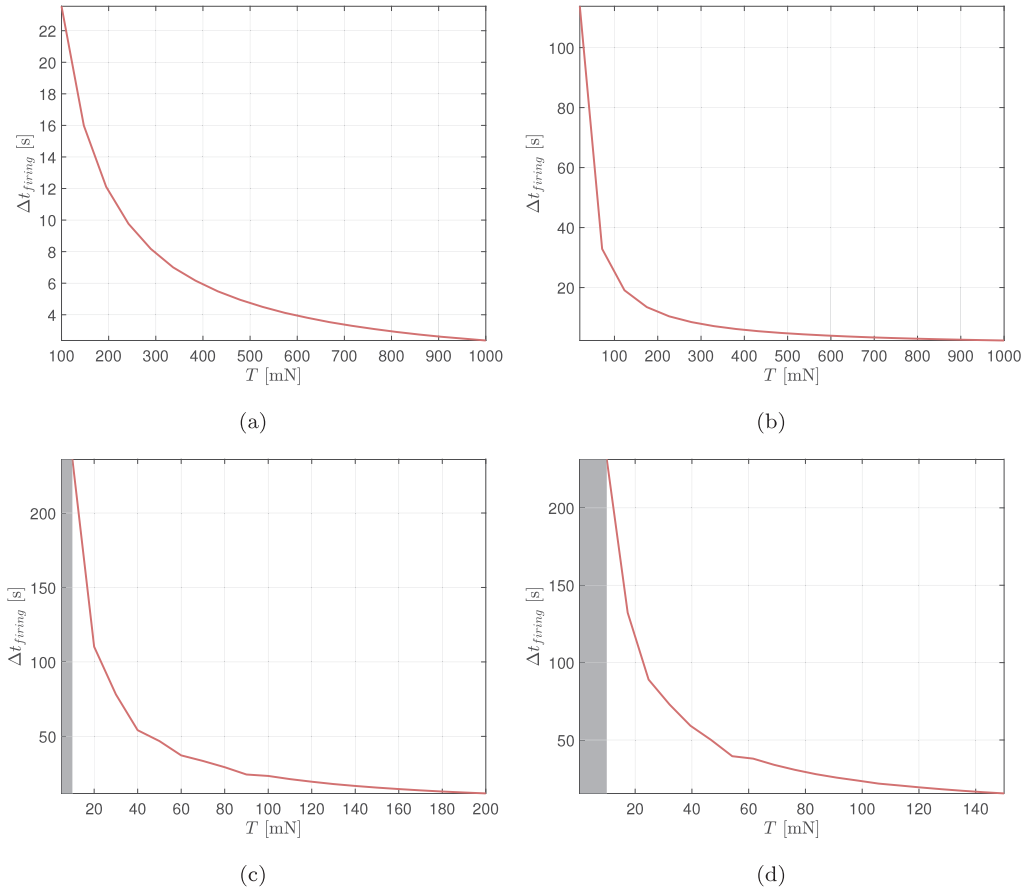

Fig. 10. Variable thrust analysis for asteroid (101955) Bennu considering different propulsion systems, namely (a) bipropellant, (b) monopropellant, (c) cold gas, and (d) resistojet.

slowly at greater distances, enabling actuators to control and track the desired attitude profile more effectively (see Figs. 12–14).

4.4. Comparison

This section discusses the different bodies considered in the analyses. By examining an increasing value of the gravitational constant, several conclusions can be drawn. Using the methodology employed in this work, it is evident that as the gravitational constant of the body increases, the minimum thrust required to allow feasible trajectories also increases. This behavior can be attributed to the stronger gravitational field, which requires higher thrust to overcome the gravitational pull and maintain a hyperbolic trajectory.

Similarly, the observation time percentage, firing time, and propellant consumption percentage also show an increasing trend as the gravitational constant increases. This is because a stronger gravitational field demands more control effort and propellant usage to maintain the desired trajectory.

In contrast, pointing accuracy is the only parameter that decreases with an increasing gravitational constant. This reduction can be attributed to the slower evolution of the trajectory under a stronger gravity field, which makes it easier for the actuators to maintain precise attitude control.

4.5. Effect of high-fidelity gravitational model

All the analyses presented in this work were performed considering a point mass gravity field. This section provides evidence that the body shape does not significantly influence the outcomes of the study. From the variable distance analysis, the orbits at the minimum distance, specifically $3R_{SB}$, were re-optimized considering the shape of the bodies. The choice on the low altitude trajectories was made because the body shape is most influential in this scenario. The irregular gravity field was modeled using the Mascon model:

$$\mathbf{a}_b = A_{BN}^{SB} \sum_{i=1}^{n} -\frac{\mu_i}{r_i^3}\mathbf{r}_i \tag{47}$$

where r_i is the distance between the center of mass of the ith tetrahedron and the spacecraft position in the asteroid body-fixed frame, and A_{BN}^{SB} is the rotation matrix from the small body body-fixed frame to the inertial frame, assuming the body rotates around its z-axis.

Two solutions are presented: the first for asteroid (99942) Apophis with a resistojet propulsion system, and the second for comet 67P/Churyumov–Gerasimenko with a bipropellant propulsion system. Both solutions use the average thrust values within the thruster ranges considered. The absolute differences between the performance metrics for the point mass and Mascon models are summarized in Table 8. As shown in the table, the differences are not particularly significant for mission design purposes. However, the discrepancies are slightly larger for 67P/Churyumov–Gerasimenko due to its highly irregular shape and stronger gravitational field. Figs. 15 and 16 illustrate the trajectories for both optimizations and the distance Δr between the two.

Table 8
Differences in performance metrics between the point mass and Mascon models.

Body	Δt_f [s]	$\Delta \eta_{obs}$ [%]	Δm_p [%]	$\Delta \delta_{point}$ [deg]
(99942) Apophis	0.4693	0.0049	0.0024	0.0059
67P/Churyumov–Gerasimenko	1.9902	0.1928	0.0446	0.0174

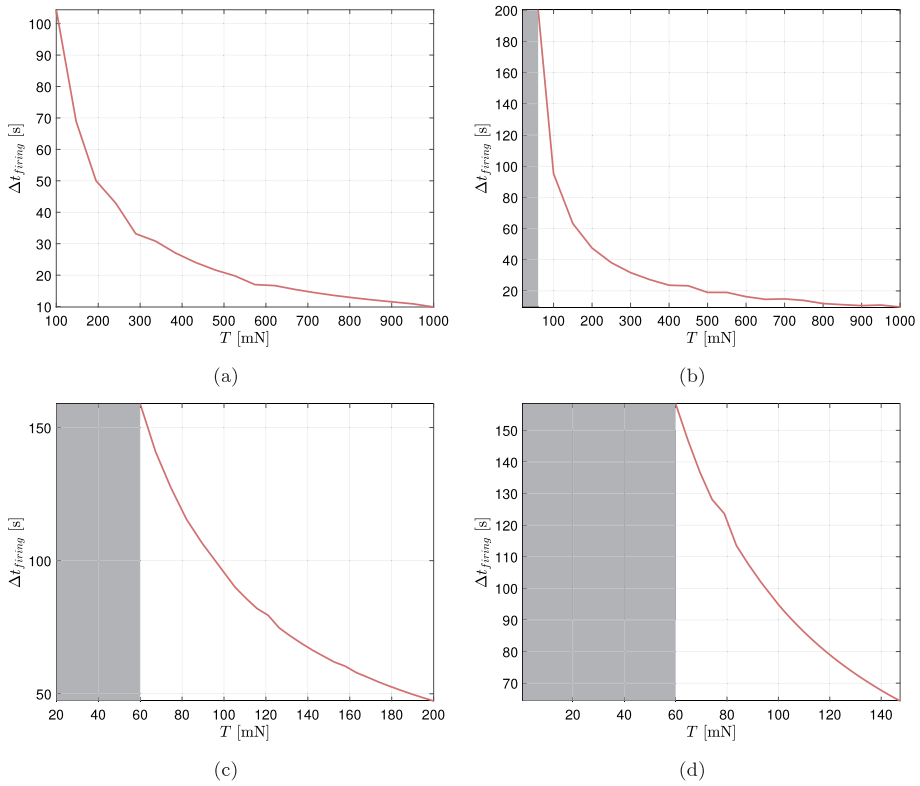

Fig. 11. Variable thrust analysis for comet 67P/Churyumov–Gerasimenko considering different propulsion systems, namely (a) bipropellant, (b) monopropellant, (c) cold gas, and (d) resistojet.

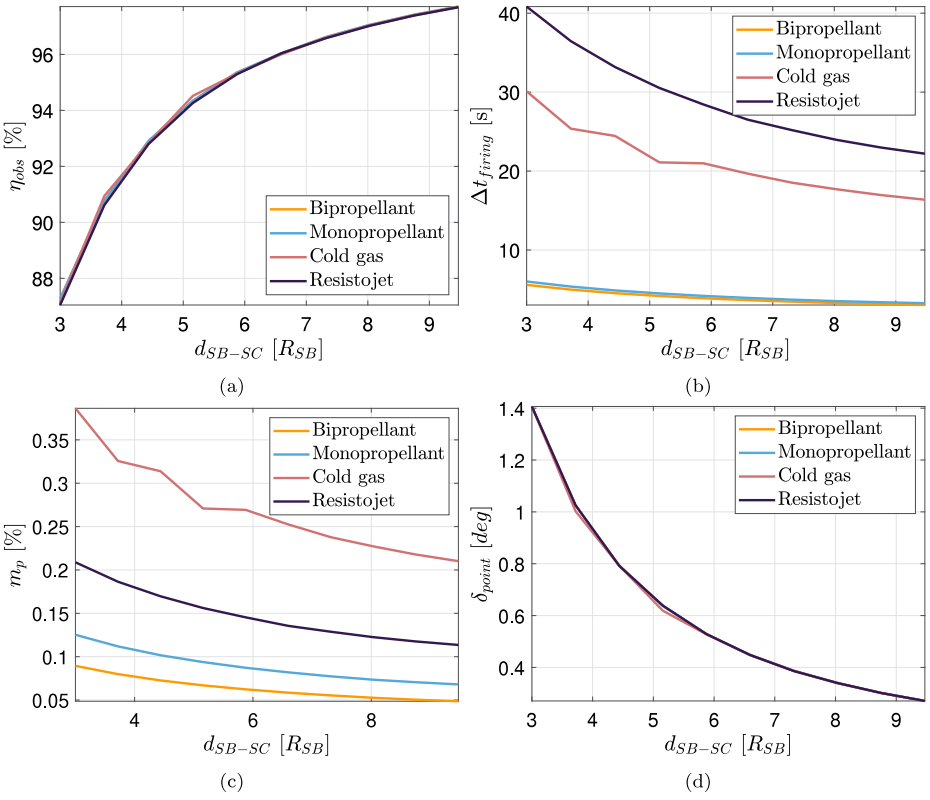

Fig. 12. Variable distance analysis for asteroid (99942) Apophis, showing performance metrics: (a) observation time percentage, (b) firing duration, (c) propellant consumption, and (d) pointing accuracy for the four propulsion systems evaluated.

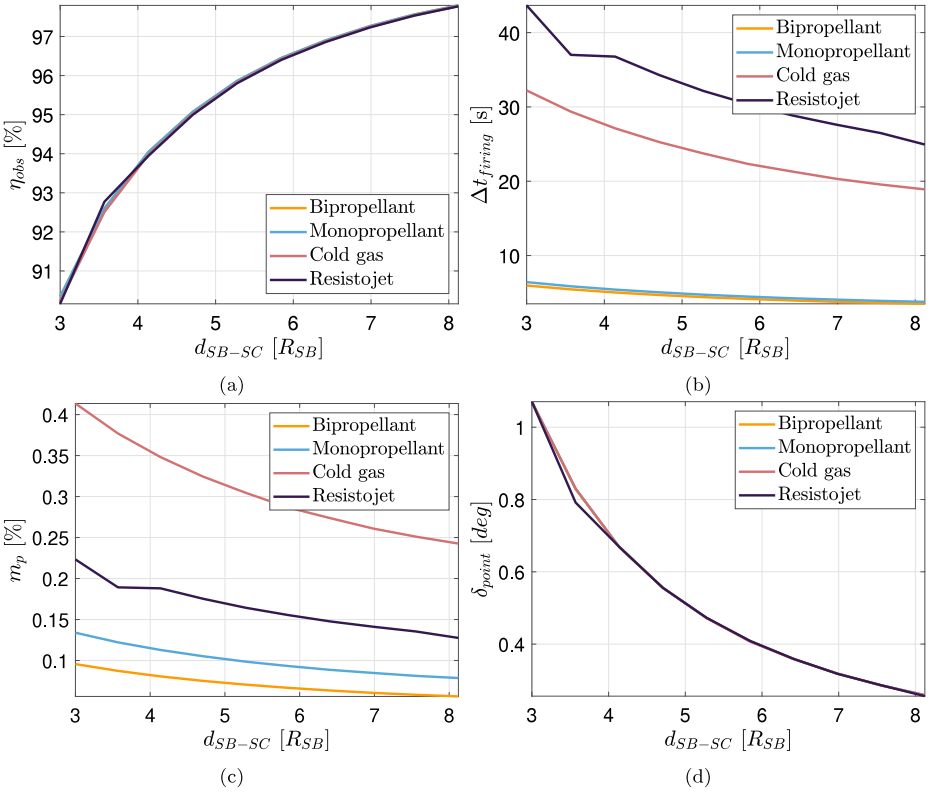

Fig. 13. Variable distance analysis for asteroid (101955) Bennu, showing performance metrics: (a) observation time percentage, (b) firing duration, (c) propellant consumption, and (d) pointing accuracy for the four propulsion systems evaluated.

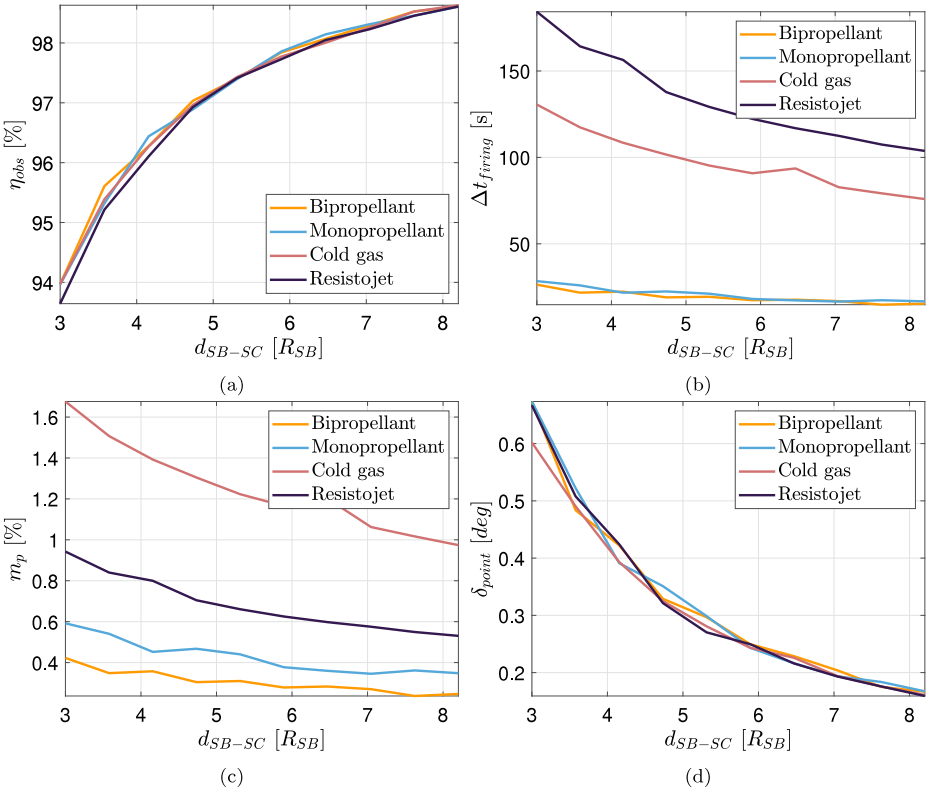

Fig. 14. Variable distance analysis for comet 67P/Churyumov–Gerasimenko, showing performance metrics: (a) observation time percentage, (b) firing duration, (c) propellant consumption, and (d) pointing accuracy for the four propulsion systems evaluated.

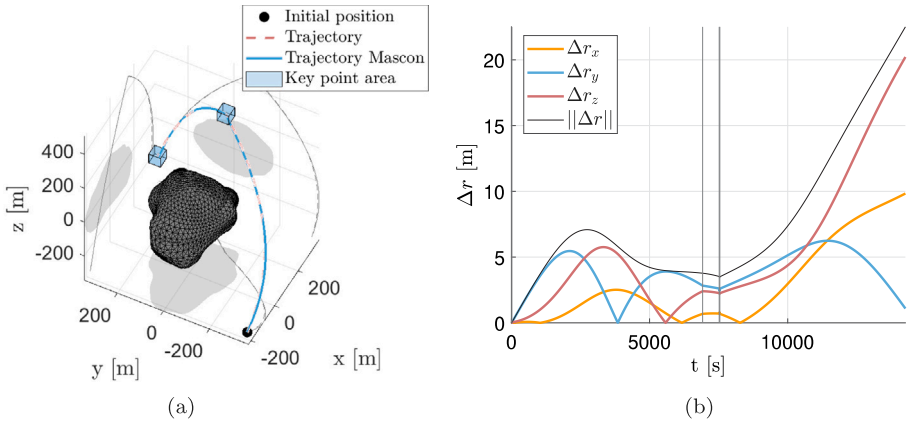

Fig. 15. Optimized trajectory using the Mascon model at a distance of $3R_{SB}$ with a resistojet propulsion system providing 75.25 mN thrust for asteroid (99942) Apophis. (a) 3D plot and (b) distance between the trajectories obtained with the two gravity models.

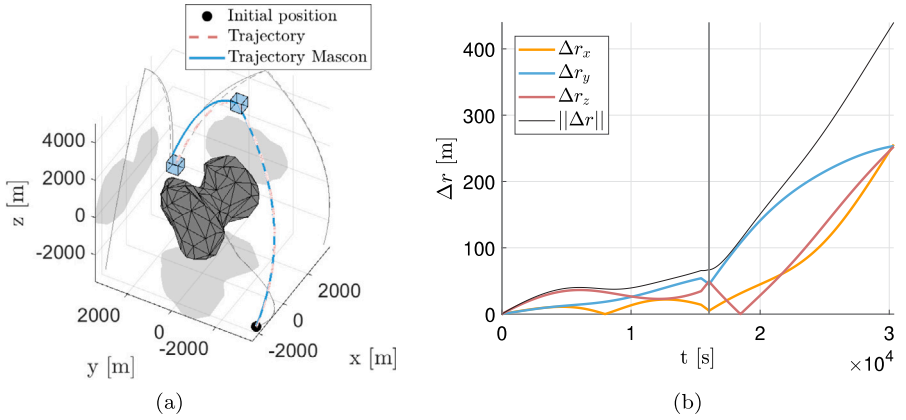

Fig. 16. Optimized trajectory using the Mascon model at a distance of $3R_{SB}$ with a bipropellant propulsion system providing 550 mN thrust for comet 67P/Churyumov–Gerasimenko. (a) 3D plot and (b) distance between the trajectories obtained with the two gravity models.

5. Conclusion

A 6-DoF optimization problem was solved to evaluate the feasibility of flying hyperbolic arcs in the proximity minor bodies, considering various propulsion systems and body properties.

The analysis highlights key considerations for selecting propulsion systems for hyperbolic arcs near minor bodies. With a minimum feasible thrust of 8 mN, electric propulsion is unsuitable for such trajectories. Additionally, not all thrust ranges of cold gas and resistojet systems are viable, as their feasibility is strongly influenced by the gravitational constant of the minor body. For any chosen propulsion system, increasing thrust leads to a reduction in firing time, while observation time, propellant consumption, and pointing accuracy remain relatively constant. Furthermore, increasing the distance from the minor body reduces firing time, allowing for longer observation periods and decreasing propellant consumption. This also improves pointing accuracy due to the slower evolution of the trajectory. The effects of high-fidelity gravitational models have been assessed, demonstrating that they are not significant for preliminary mission design.

In summary, this work provides insights for selecting propulsion systems for hyperbolic trajectories near minor bodies, assisting mission designers in the preliminary estimation of mission performance and costs.

CRediT authorship contribution statement

Carmine Buonagura: Software, Funding acquisition, Writing – review & editing, Methodology, Formal analysis, Writing – original draft, Investigation. **Carmine Giordano:** Supervision, Conceptualization, Methodology, Writing – review & editing, Funding acquisition. **Angelo Cervone:** Supervision, Funding acquisition, Writing – review & editing. **Francesco Topputo:** Supervision, Funding acquisition.

Declaration of competing interest

The authors declare that they have no known competing financial interests or personal relationships that could have appeared to influence the work reported in this paper.

Acknowledgments

This work was supported by the IDEA League Student Grants 2024.

This work was partially carried out as part of CASTOR, a project that has received funding from the European Union's Horizon Europe research and innovation programme under the Marie Skłodowska-Curie grant agreement no. 101103826.

References

[1] E. Asphaug, Growth and evolution of asteroids, Annu. Rev. Earth Planet. Sci. 37 (2009) 413–448, http://dx.doi.org/10.1146/ANNUREV.EARTH.36.031207.124214.

[2] M. Quadrelli, L. Wood, J. Riedel, M. McHenry, M. Aung, L. Cangahuala, R. Volpe, P. Beauchamp, J. Cutts, Guidance, navigation, and control technology assessment for future planetary science missions, J. Guid. Control Dyn. 38 (7) (2015) 1165–1186, http://dx.doi.org/10.2514/1.G000525.

[3] K. Zacny, P. Chu, J. Craft, M. Cohen, W. James, B. Hilscher, Asteroid mining, in: AIAA SPACE 2013 Conference and Exposition, 2013.

[4] W.F. Bottke Jr., A. Cellino, P. Paolicchi, R.P. Binzel, An overview of the asteroids: The asteroids III perspective, Asteroids III 1 (2002) 3–15.
[5] D. Morrison, Asteroid sizes and albedos, Icarus 31 (2) (1977) 185–220, http://dx.doi.org/10.1016/0019-1035(77)90034-3.
[6] C. Buonagura, C. Giordano, F. Ferrari, F. Topputo, The orbital Regime index: A comprehensive parameter to determine orbital regions around minor bodies, in: 47th Rocky Mountain AAS GN&C Conference, 2024.
[7] R. Walker, D. Binns, C. Bramanti, M. Casasco, P. Concari, D. Izzo, D. Feili, P. Fernandez, J.G. Fernandez, P. Hager, et al., Deep-space CubeSats: Thinking inside the box, Astron. Geophys. 59 (5) (2018) 5–24, http://dx.doi.org/10.1093/astrogeo/aty237.
[8] F. Topputo, Y. Wang, C. Giordano, V. Franzese, H. Goldberg, F. Perez-Lissi, R. Walker, Envelop of reachable asteroids by M-ARGO CubeSat, Adv. Space Res. 67 (12) (2021) 4193–4221, http://dx.doi.org/10.1016/j.asr.2021.02.031.
[9] A.S. French, Y. Takahashi, R.L. Anderson, S. Bhaskaran, S. Bandyopadhyay, R. Amini, Navigating a dual-spacecraft bistatic radar around an asteroid, in: 33rd AAS/AIAA Space Flight Mechanics Meeting, 2023.
[10] L. Prockter, S. Murchie, A. Cheng, S. Krimigis, R. Farquhar, A. Santo, J. Trombka, The NEAR Shoemaker mission to asteroid 433 eros, Acta Astronaut. 51 (1) (2002) 491–500, http://dx.doi.org/10.1016/S0094-5765(02)00098-X.
[11] M. Yoshikawa, J. Kawaguchi, A. Fujiwara, A. Tsuchiyama, Hayabusa sample return mission, Asteroids IV 1 (1) (2015) http://dx.doi.org/10.2458/azu_uapress_9780816532131-ch021.
[12] C.T. Russell, C.A. Raymond, The dawn mission to vesta and ceres, in: The Dawn Mission to Minor Planets 4 Vesta and 1 Ceres, Springer New York, New York, NY, 2012, pp. 3–23, http://dx.doi.org/10.1007/978-1-4614-4903-4_2.
[13] K.-H. Glassmeier, H. Boehnhardt, D. Koschny, E. Kührt, I. Richter, The Rosetta mission: Flying towards the origin of the solar system, Space Sci. Rev. 128 (2007) 1–21, http://dx.doi.org/10.1007/s11214-006-9140-8.
[14] S.-i. Watanabe, Y. Tsuda, M. Yoshikawa, S. Tanaka, T. Saiki, S. Nakazawa, Hayabusa2 mission overview, Space Sci. Rev. 208 (2017) 3–16, http://dx.doi.org/10.1007/s11214-017-0377-1.
[15] D.S. Lauretta, S.S. Balram-Knutson, E. Beshore, W.V. Boynton, C. Drouet d'Aubigny, D.N. DellaGiustina, H.L. Enos, D.R. Golish, C.W. Hergenrother, E.S. Howell, C.A. Bennett, E.T. Morton, M.C. Nolan, B. Rizk, H.L. Roper, A.E. Bartels, B.J. Bos, J.P. Dworkin, D.E. Highsmith, D.A. Lorenz, L.F. Lim, R. Mink, M.C. Moreau, J.A. Nuth, D.C. Reuter, A.A. Simon, E.B. Bierhaus, B.H. Bryan, R. Ballouz, O.S. Barnouin, R.P. Binzel, W.F. Bottke, V.E. Hamilton, K.J. Walsh, S.R. Chesley, P.R. Christensen, B.E. Clark, H.C. Connolly, M.K. Crombie, M.G. Daly, J.P. Emery, T.J. McCoy, J.W. McMahon, D.J. Scheeres, S. Messenger, K. Nakamura-Messenger, K. Righter, S.A. Sandford, OSIRIS-REx: Sample return from asteroid (101955) Bennu, Space Sci. Rev. 212 (2017) 925—984, http://dx.doi.org/10.1007/s11214-017-0405-1.
[16] E. Dotto, V. Della Corte, M. Amoroso, I. Bertini, J.R. Brucato, A. Capannolo, B. Cotugno, G. Cremonese, V. Di Tana, I. Gai, S. Ieva, G. Impresario, S.L. Ivanovski, M. Lavagna, A. Lucchetti, E. Mazzotta Epifani, A. Meneghin, F. Miglioretti, D. Modenini, M. Pajola, P. Palumbo, D. Perna, S. Pirrotta, G. Poggiali, A. Rossi, E. Simioni, S. Simonetti, P. Tortora, M. Zannoni, G. Zanotti, A. Zinzi, A.F. Cheng, A.S. Rivkin, E.Y. Adams, E.L. Reynolds, K. Fretz, Liciacube — The light Italian cubesat for imaging of asteroids in support of the NASA DART mission towards asteroid (65803) Didymos, Planet. Space Sci. 199 (2021) 105185, http://dx.doi.org/10.1016/j.pss.2021.105185.
[17] M. Pugliatti, A. Rizza, F. Piccolo, V. Franzese, C. Bottiglieri, C. Giordano, F. Ferrari, F. Topputo, The milani mission: Overview and architecture of the optical-based gnc system, in: AIAA SCITECH 2022 Forum, 2022.
[18] H. Goldberg, Ö. Karatekin, B. Ritter, A. Herique, P. Tortora, C. Prioroc, B.G. Gutierrez, P. Martino, I. Carnelli, The juventas CubeSat in support of ESA's hera mission to the asteroid Didymos, in: 33rd Annual AIAA/USU Conference on Small Satellites, 2019.
[19] P. Michel, M. Kueppers, H. Sierks, I. Carnelli, A.F. Cheng, K. Mellab, M. Granvik, M. Kestilä, T. Kohout, K. Muinonen, A. Näsilä, A. Penttila, T. Tikka, P. Tortora, V. Ciarletti, A. Hérique, N. Murdoch, E. Asphaug, A. Rivkin, O. Barnouin, A.C. Bagatin, P. Pravec, D.C. Richardson, S.R. Schwartz, K. Tsiganis, S. Ulamec, O. Karatekin, European component of the AIDA mission to a binary asteroid: Characterization and interpretation of the impact of the DART mission, Adv. Space Res. 62 (8) (2018) 2261–2272, http://dx.doi.org/10.1016/j.asr.2017.12.020.
[20] S.P. Naidu, L.A.M. Benner, M. Brozovic, M.C. Nolan, S. Ostro, J.L. Margot, J.D. Giorgini, T. Hirabayashi, D.J. Scheeres, P. Pravec, P. Scheirich, C. Magri, J.S. Jao, Radar observations and a physical model of binary near-Earth asteroid 65803 Didymos, target of the DART mission, Icarus 348 (2020) 113777, http://dx.doi.org/10.1016/j.icarus.2020.113777.
[21] R.T. Daly, C.M. Ernst, O.S. Barnouin, R.W. Gaskell, H. Nair, H. Agrusa, N.L. Chabot, A.F. Cheng, E. Dotto, E.M. Epifani, R.C. Espiritu, T.L. Farnham, E.E. Palmer, P. Pravec, A.S. Rivkin, D.C. Waller, A. Zinzi, the DART, L. teams, An updated shape model of dimorphos from DART data, Planet. Sci. J. 5 (1) (2024) 24, http://dx.doi.org/10.3847/PSJ/ad0b07.
[22] M. Kueppers, P. Martino, I. Carnelli, P. Michel, Ramses–ESA's study for a small mission to apophis, in: AAS/Division for Planetary Sciences Meeting Abstracts, vol. 55, 2023, pp. 201–208.
[23] R.B. Negri, A.F.B.A. Prado, R.A.J. Chagas, R.V. Moraes, Autonomous rapid exploration in close-proximity of asteroids, J. Guid. Control Dyn. 47 (5) (2024) 914–933, http://dx.doi.org/10.2514/1.G007186.
[24] S. Takahashi, D.J. Scheeres, Autonomous exploration of a small near-earth asteroid, J. Guid. Control Dyn. 44 (4) (2021) 701–718, http://dx.doi.org/10.2514/1.G005733.
[25] R. Furfaro, D. Cersosimo, D.R. Wibben, Asteroid precision landing via multiple sliding surfaces guidance techniques, J. Guid. Control Dyn. 36 (4) (2013) 1075–1092, http://dx.doi.org/10.2514/1.58246.
[26] R. Furfaro, Hovering in asteroid dynamical environments using higher-order sliding control, J. Guid. Control Dyn. 38 (2) (2015) 263–279, http://dx.doi.org/10.2514/1.G000631.
[27] F. Ferrari, V. Franzese, M. Pugliatti, C. Giordano, F. Topputo, Trajectory options for Hera's Milani cubesat around (65803) Didymos, J. Astronaut. Sci. 68 (4) (2021) 973–994, http://dx.doi.org/10.1007/s40295-021-00282-z.
[28] C. Bottiglieri, F. Piccolo, C. Giordano, F. Ferrari, F. Topputo, Applied trajectory design for CubeSat close-proximity operations around asteroids: The milani case, Aerospace 10 (5) (2023) http://dx.doi.org/10.3390/aerospace10050464.
[29] B. Gaudet, R. Linares, R. Furfaro, Terminal adaptive guidance via reinforcement meta-learning: Applications to autonomous asteroid close-proximity operations, Acta Astronaut. 171 (2020) 1–13, http://dx.doi.org/10.1016/j.actaastro.2020.02.036.
[30] D. Dumitriu, P.U. Lima, B. Udrea, Optimal trajectory planning of formation flying spacecraft, 38, (1) 2005, pp. 313–318,
[31] Y. Chihabi, S. Ulrich, Software-in-the-loop validation of a novel two-point optimal guidance for perturbed spacecraft rendezvous and formations, J. Astronaut. Sci. 70 (5) (2023) 1–45, http://dx.doi.org/10.1007/s40295-023-00405-8.
[32] J.-F. Hamel, J. de Lafontaine, Neighboring optimum feedback control law for earth-orbiting formation-flying spacecraft, J. Guid. Control Dyn. 32 (1) (2009) 290–299, http://dx.doi.org/10.2514/1.32778.
[33] D.A. Dei Tos, M. Rasotto, F. Renk, F. Topputo, LISA Pathfinder mission extension: A feasibility analysis, Adv. Space Res. 63 (12) (2019) 3863–3883, http://dx.doi.org/10.1016/j.asr.2019.02.035.
[34] D.A. Dei Tos, F. Topputo, High-fidelity trajectory optimization with application to saddle-point transfers, J. Guid. Control Dyn. 42 (6) (2019) 1343–1352, http://dx.doi.org/10.2514/1.G003838.
[35] R.H. Battin, Solving Lambert's problem, in: An Introduction to the Mathematics and Methods of Astrodynamics, Revised Edition, AIAA, 1999, pp. 295–364, http://dx.doi.org/10.2514/5.9781600861543.0295.0364.
[36] S. Alnaqbi, D. Darfilal, S.S.M. Swei, Propulsion technologies for CubeSats: Review, Aerospace 11 (7) (2024) http://dx.doi.org/10.3390/aerospace11070502.